Shear Capacity as Prognostic for Nocturnal Boundary Layer Regimes

IVO G. S. VAN HOOIJDONK, JUDITH M. M. DONDA, AND HERMAN J. H. CLERCX

Fluid Dynamics Laboratory, and J.M. Burgerscentrum, Eindhoven University of Technology, Eindhoven, Netherlands

FRED C. BOSVELD

Royal Netherlands Meteorological Institute, De Bilt, Netherlands

BAS J. H. VAN DE WIEL

Fluid Dynamics Laboratory, and J.M. Burgerscentrum, Eindhoven University of Technology, Eindhoven, Netherlands

(Manuscript received 30 April 2014, in final form 10 November 2014)

ABSTRACT

Field observations and theoretical analysis are used to investigate the appearance of different nocturnal boundary layer regimes. Recent theoretical findings predict the appearance of two different regimes: the continuously turbulent (weakly stable) boundary layer and the relatively ''quiet'' (very stable) boundary layer. A large number of nights (approximately 4500 in total) are analyzed using an ensemble averaging technique. The observations support the existence of these two fundamentally different regimes: weakly stable (turbulent) nights rapidly reach a steady state (within 2–3 h). In contrast, very stable nights reach a steady state much later after a transition period (2–6 h). During this period turbulence is weak and nonstationary. To characterize the regime, a new parameter is introduced: the shear capacity. This parameter compares the actual shear after sunset with the minimum shear needed to sustain continuous turbulence. In turn, the minimum shear is dictated by the heat flux demand at the surface (net radiative cooling), so that the shear capacity combines flow information with knowledge of the boundary condition. It is shown that the shear capacity enables prediction of the flow regimes. The prognostic strength of this nondimensional parameter appears to outperform the traditional ones like the similarity parameter z/L and the gradient Richardson number R_i as a regime indicator.

1. Introduction

In the present work, a systematic analysis of field observations from the Royal Netherlands Meteorological Institute (KNMI) Cabauw tower (the Netherlands) is performed in order to study nocturnal boundary layer regimes. It will be shown that two qualitatively different regimes occur and that their appearance can be explained in terms of a hypothesis introduced recently by van de Wiel et al. (2012a,b, hereafter VDW12a,b). This theory couples ambient flow characteristics with aspects of the surface energy budget in order to explain regime transitions.

It is generally known that nocturnal boundary layers (NBLs), which occur under windy conditions, called weakly stable boundary layers, largely differ from so-called very stable boundary layers, with weak winds and clear skies (e.g., Mahrt 2014; VDW12a,b; Mauritsen et al. 2007; Grachev et al. 2005; Monahan et al. 2011). Whereas turbulence in the first case is relatively strong and continuous, it tends to be weak and intermittent in the latter (e.g., Acevedo and Fitzjarrald 2000; Sun et al. 2004).

In the past, attempts have been made to relate the occurrence of those regimes to local stability parameters like the gradient Richardson number [$R_i = (g/\theta_0)(\partial\theta/\partial z)/(\partial U/\partial z)$, where g is gravity, θ is the potential temperature, z is height, and U is the wind speed] or the similarity parameter z/L, where L is the Obukhov length (e.g., Mahrt et al. 1998). Broadly speaking, weakly stable boundary layers tend to coincide with low values of R_i

Denotes Open Access content.

Corresponding author address: I. G. S. van Hooijdonk, Fluid Dynamics Laboratory, Eindhoven University of Technology, Den Dolech 2, 5612 AZ Eindhoven, Netherlands.
E-mail: i.g.s.v.hooijdonk@tue.nl

DOI: 10.1175/JAS-D-14-0140.1

and z/L and very stable boundary layers with high values. Despite this, data stratification in terms of those stability parameters has been only partly successful. This can be explained by the fact that response of the boundary layer as a whole is not uniquely related to the value of a local stability parameter (i.e., for a given L, z could be anything depending on the height of the observations).

To avoid usage of local parameters, one could try to relate the occurrence of boundary layer regimes to "external" parameters like the geostrophic wind and net radiative surface cooling. Although this approach has been promising to some extent (Derbyshire 1999; van de Wiel et al. 2003; Acevedo and Fitzjarrald 2000; Łobocki 2013), it has limiting perspective for analyzing field observations in practice. This is due to the fact that the synoptic pressure gradient is not a directly observed quantity in the field. This makes analysis of the geostrophic wind a nontrivial exercise (e.g., baroclinic effects may become important). Also, for weak wind conditions the geostrophic wind is less correlated to the magnitude of the wind speed in the stable boundary layer (SBL). Therefore, the initial wind speed (i.e., at sunset) is used as external wind forcing. With respect to net radiation, the following has to be considered: strictly speaking, it is an internal parameter that depends on both the air and surface temperature (Edwards 2009). To eliminate this dependency, one could utilize the so-called isothermal net radiation, as defined in Monteith (1981) and Holtslag and de Bruin (1988). However, in practice, the magnitude of the radiative budget is largely determined by the amount of cloud coverage. For practical reasons, we therefore consider net radiation as an external forcing in the remainder of this work (for a complete discussion, we refer to VDW12a).

Here, we present an alternative route that does not need the geostrophic wind as an input parameter for regime classification. It builds on the maximum sustainable heat flux hypothesis (MHF) as presented in VDW12a and VDW12b. The sketch in Fig. 1 illustrates this hypothesis: thermal balance at a surface with low heat capacity (e.g., short grass or snow) can be reached if the turbulent heat flux (at least approximately) balances the energy demand, which is the net radiative cooling Q_N minus the soil heat flux G (both taken constant for simplicity; black dashed line in Fig. 1). Also for simplicity the latent heat flux is assumed negligible.

For a given shear, the downward heat flux $|H|$ maximizes at moderate stability in stratified flows: the heat flux becomes small in both the neutral limit (small temperature gradient) and the very stable limit (weak mixing). This general characteristic has been reported in many studies and is readily derived within the framework of Monin–Obukhov (MO) similarity (see section 4 and references therein).

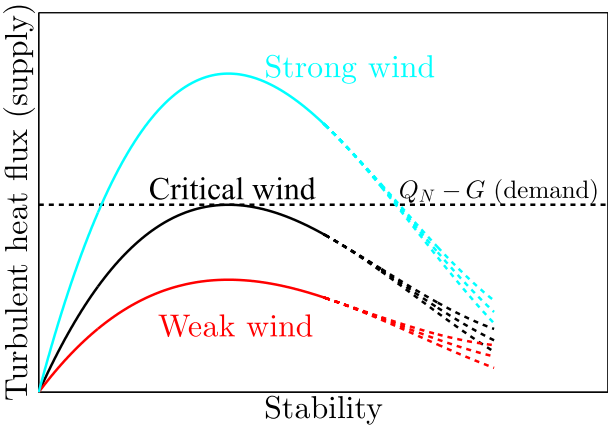

FIG. 1. Sketch of the turbulent heat flux curve vs stability for weak winds (red), the minimum ("critical") wind (black), and strong winds (blue). The energy demand is given by the dashed line. Here, $|Q_N|$ is the net radiative heat loss at the surface. The soil heat flux $|G|$ is incorporated in the demand. For strong stability levels, Monin–Obukhov similarity is no longer valid (e.g., Mahrt 2014); as a result, the shape of the curves becomes uncertain.

The value of this maximum itself strongly depends on the magnitude of the ambient shear. Here, it is clear that no balance can be reached in the case of weak winds (red curve) as even the maximum heat flux supply is less than the energy demand. As such, the surface temperature decreases, hence stability increases. This positive feedback loop generally leads to strongly suppressed levels of turbulence (e.g., Flores and Riley 2011; Ansorge and Mellado 2014).

In the other extreme, if the wind is strong, then the supply and demand can be in balance (blue curve). As such, we can find an intermediate "critical" wind strength (black curve) where the wind is just strong enough so that the maximum heat flux compensates the net radiative loss at the surface (or a predefined fraction of it). This wind strength is the minimum wind (shear) strength to sustain turbulence. This minimum shear defines a characteristic velocity scale, which will be used for normalization of the actual shear in our dataset. This nondimensional shear will be coined the shear capacity of the flow (SC).

In the reasoning above, it is assumed that, for turbulence to survive, the thermal balance at the surface should be reached rapidly. It does not account for flow acceleration effects (e.g., formation of the low-level jet), so that the ambient shear is considered "fixed." As such, the analysis is mainly focused on the first few hours (0–3 h) after sunset. On the other hand, it is expected that an initial collapse of turbulence in the beginning of the night will favor flow acceleration during the night. This acceleration, in turn, increases the chance of turbulence to be regenerated later that night (e.g., Businger et al. 1971 and Donda et al. 2015). This interesting aspect of

time dependence will also be given attention in the present work.

The observational analysis utilizes a large dataset (approximately 10 years) of the 200-m tower at the Cabauw observatory of KNMI (van Ulden and Wieringa 1996). From this set, composite cases according to bins of wind classes are constructed, following the philosophy of Baas et al. (2012). In this way, each case corresponds to a group of similar nights. The approach emphasizes general characteristics of each wind class, as case-to-case variation of individual nights is largely averaged out. Furthermore, we restrict the analysis to clear-sky cases.

This paper is organized as follows: In section 2, a brief overview of the data analysis is given. In section 3, it is shown that the nights can be subdivided into two separate boundary layer regimes, which, for each height specifically, can be classified according to the ambient wind strength around sunset. Next, the concept of the shear capacity is introduced, which is then used to classify the data independent of the observational height, and a comparison between SC and z/L and R_i as regime indicators is made (section 4). In section 5 the results are interpreted using the budget of turbulent kinetic energy. Discussion and conclusions are given in sections 6 and 7, respectively.

2. Data analysis

Field observations are used, obtained at Cabauw [for description of the site, see van Ulden and Wieringa (1996) and Beljaars and Bosveld (1997)] between August 2000 and December 2012. Temperature (KNMI Pt500 element) and wind speed (cup anemometer) measurements at the main tower are obtained at 40, 80, 140, and 200 m. Auxiliary towers provide measurements at 10 and 20 m. The air temperature is also measured at 1.5 m. The net radiation is determined from the individual (shortwave and longwave, incoming and outgoing) radiation components. All fluxes are near-surface values determined from an eddy covariance technique applied to air temperature and wind speed measurements at the 5-m flux tower. Information on the instrumentation and relative position of the towers can be found in Bosveld (2014).

Our aim is to follow the methodology of Baas et al. (2012) to build composite cases. By using multinight composites (ensemble averages), random disturbances occurring in individual nights largely average out. The reduction in scatter is expected to provide a clearer view of the SBL dynamics.

The Cabauw database is divided in 24-h periods starting at 0600 local time (LT), such that each period contains a full night.

The formation of the stably stratified boundary layer is initiated by a change of sign of Q_N. Hence, cases (24-h periods) are "synchronized" by setting time t to 0 h when Q_N changes sign from positive to negative. Depending on the season, this generally occurs between 1500 and 1900 LT, several hours before the astronomical sunset.

TABLE 1. Overview of the number of nights per class.

Class ($m\,s^{-1}$)	N	Class ($m\,s^{-1}$)	N
$U_{40} \in [1.0; 1.5]$	28	$U_{40} \in [5.5; 6.0]$	144
$U_{40} \in [1.5; 2.0]$	44	$U_{40} \in [6.0; 6.5]$	72
$U_{40} \in [2.0; 2.5]$	47	$U_{40} \in [6.5; 7.0]$	100
$U_{40} \in [2.5; 3.0]$	71	$U_{40} \in [7.0; 7.5]$	75
$U_{40} \in [3.0; 3.5]$	93	$U_{40} \in [7.5; 8.0]$	72
$U_{40} \in [3.5; 4.0]$	102	$U_{40} \in [8.0; 8.5]$	59
$U_{40} \in [4.0; 4.5]$	128	$U_{40} \in [8.5; 9.0]$	45
$U_{40} \in [4.5; 5.0]$	139	$U_{40} \in [9.0; 9.5]$	28
$U_{40} \in [5.0; 5.5]$	149	$U_{40} \in [9.5; 10.0]$	15

A filter selects nights with clear skies—that is, an average net radiation $|Q_N| > 30\,W\,m^{-2}$ and a standard deviation (with respect to the average of a particular night) $\sigma_Q < 15\,W\,m^{-2}$. Each night is classified according to the mean presunset wind speed at 40 m U_{40} between times $t = -4$ and $t = 0$ h. Note that the classification appears to be insensitive to the exact choice for time and altitude. Among nights with clear skies, the variation of the radiative forcing is relatively weak. Additionally, dynamics appear to be less sensitive to radiative forcing compared to the mechanical forcing (Sun et al. 2012). Therefore, only the wind speed is used for classification purposes here.

Table 1 shows that the number of nights N in each class is relatively large. For each class, the night with the shortest time span occurs in summer. This restricts our composite analysis to $t < 9$ h.

3. Two regimes

Here, several composite quantities (mean wind and temperature profiles, turbulent fluxes) are analyzed. In this section, it is shown that a clear distinction in two qualitatively different regimes can be made: a weakly stable regime and a very stable regime. We base ourselves on section 3d to make the regime division at $U_{40} \approx 5.5\,m\,s^{-1}$ in all figures for this dataset. For wind speed classes (Table 1) above $5.5\,m\,s^{-1}$, a more or less stationary weakly stable boundary layer regime sets in, whereas for lower wind speed, a nonstationary, very stable boundary layer occurs.

a. Temporal evolution of mean wind profiles

Figures 2a–d show the wind profiles for two very stable cases ($U_{40} \in [1.0; 1.5]\,m\,s^{-1}$, $U_{40} \in [2.0; 2.5]\,m\,s^{-1}$, Figs. 2a,b; see Table 1) and two weakly stable cases ($U_{40} \in [5.5; 6.0]\,m\,s^{-1}$ and $U_{40} \in [8.0; 8.5]\,m\,s^{-1}$, Figs. 2c,d); unless it is unclear from the text, we will omit the explicit

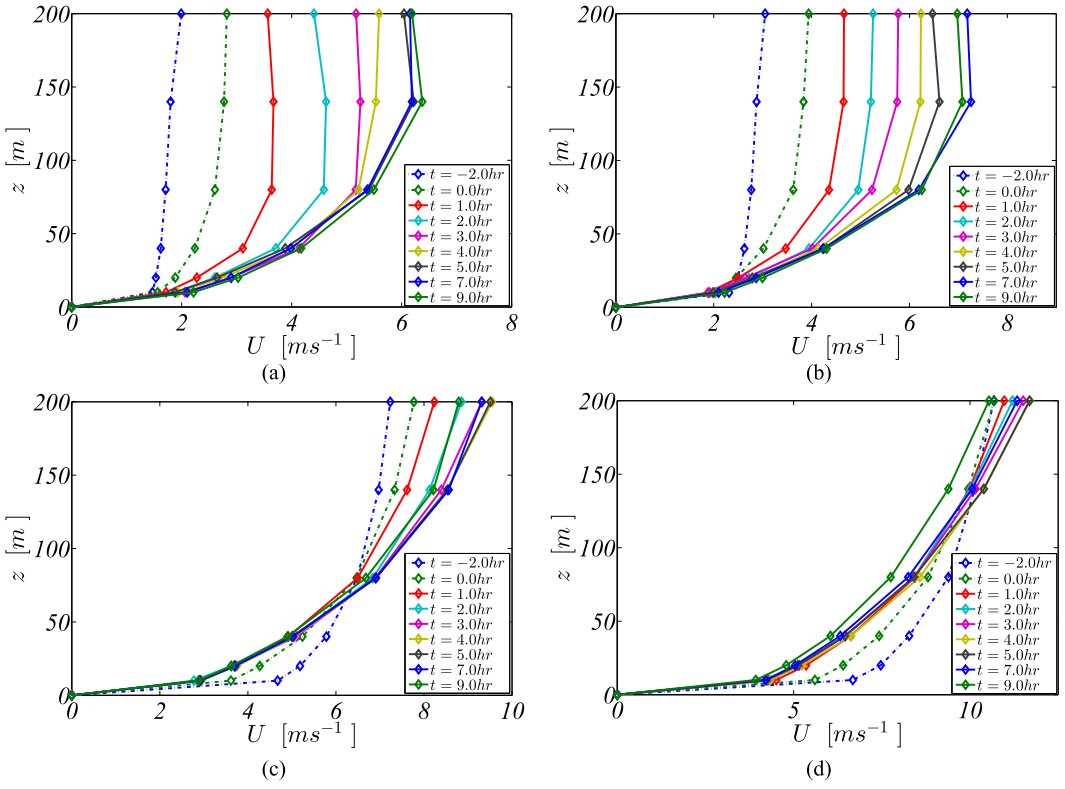

FIG. 2. Wind speed profiles for $t \in [-2; 9]$ h of four classes of the presunset U_{40} (Table 1) (a) [1.0; 1.5], (b) [2.0; 2.5], (c) [5.5; 6.0], and (d) [8.0; 8.5] m s^{-1}. The diamonds represent ensemble-averaged measurements. The lines are linear interpolations.

reference to U_{40} as either a classification parameter or a diagnosed quantity from here on. For the weakly stable cases, the wind profiles are reasonably steady after 3 h (i.e., after sunset). The consistency in the steady-state profile reflects that indeed significant reduction of scatter is achieved by using the composite method.

For the weakly stable cases, in the first decameters above the surface, the steady state is formed within 1–3 h. The thickness of this layer increases with wind speed class. For example, in Fig. 2c the thickness is approximately 60 m; in Fig. 2d the thickness is larger than 140 m. Above this layer, an acceleration is observed that can be explained by an inertial oscillation of the wind (Blackadar 1957). This phenomenon is outside of the scope of this study.

The very stable cases have not (yet) reached a steady state at $t = 3$ h. Later, however, after 4–5 h some kind of "preferred state" appears to develop. If we heuristically take 40 m as a representative level, both Figs. 2a and 2b indicate that the 40-m wind becomes steady when it reaches a value of 4–4.5 m s^{-1}. Additional inspection of other very stable cases indicates that this remarkable feature occurs in all cases (not shown here). This aspect is discussed below.

b. *Temporal evolution of turbulent stress*

In Fig. 3 the evolution of the (near surface) turbulent stress is given as a function of time after sunset. Lines are colored according to $U_{40} < 5.5$ (red) and $U_{40} > 5.5$ m s^{-1} (blue). The regime coloring is based on temperature inversion characteristics. Generally, turbulent stresses

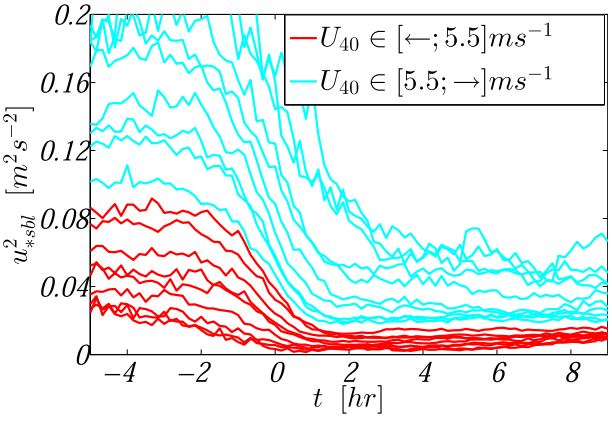

FIG. 3. The temporal evolution of the near-surface kinematic stress is shown for all classes $U_{40} \in [1.0; 10.0]$ m s^{-1}. The classes are divided into weakly stable (blue) and very stable (red) cases (see Fig. 5).

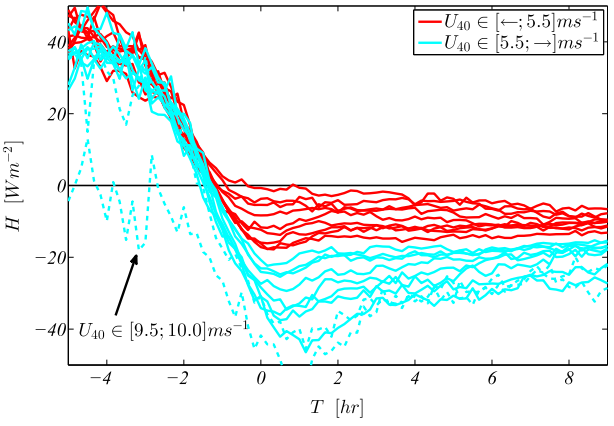

FIG. 4. The temporal evolution of the near-surface turbulent heat flux is shown for all classes $U_{40} \in [1.0; 10.0]\,\mathrm{m\,s^{-1}}$. The division into weakly stable (blue) and very stable (red) cases is made. For the very stable cases, a tendency toward a single end state is observed.

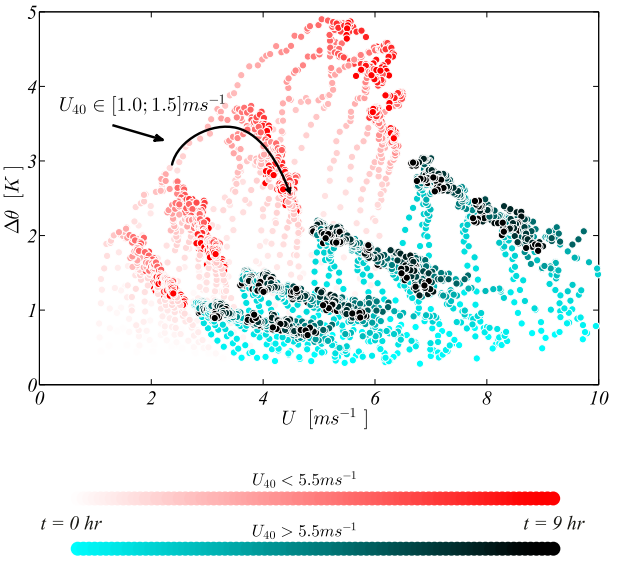

FIG. 5. The temperature inversion $\Delta\theta = \theta(z) - \theta(1.5\,\mathrm{m})$ as function of the wind speed $U(z)$ is shown for $z = 10$, 20, 40, and 80 m. Analysis reveals that the slope of all $\Delta\theta$ vs U curves is small at high initial wind speed and large at small initial wind speed. The initial U_{40} that separates the two regimes is at $5.5\,\mathrm{m\,s^{-1}}$. Hence this wind-class threshold is used to separate weakly stable cases (blue color) from very stable ones (red color). Additionally, time dependence is indicated via the color intensity (each increment to darker shades denotes a 10-min advance in time), as depicted by the color bars below the graph. For a single case ($U_{40} \in [1.0; 1.5]\,\mathrm{m\,s^{-1}}$), time evolution is indicated by the black arrow.

decrease in the afternoon owing to onset of the stable boundary layer. The weakly stable cases (blue) reach stress levels, which appear to be more or less constant. In contrast, for the very stable cases, the stresses reach a minimum just after sunset, followed by an increase (up to 300% for the most stable cases) during the night. Qualitatively, this increase agrees with the aforementioned flow acceleration (e.g., Donda et al. 2015). Again, very stable cases show a tendency to reach some kind of preferred state. Here, this state corresponds with a turbulent stress of $u_*^2 \approx 0.01\,\mathrm{m^2\,s^{-2}}$. A closer analysis of nonsummer nights only ($t > 9\,\mathrm{h}$) suggests a converging trend (not shown), though the amount of scatter (''error bars;'' not shown) somewhat increases owing to the fact that a smaller subset is used.

c. Temporal evolution of the turbulent heat flux

Similar to Fig. 3, the temporal evolution of the (near surface) turbulent heat flux is shown in Fig. 4. The same division in colors is made. Before sunset, convective mixing causes the turbulent heat flux to be very similar among wind speed classes [with the exception of the highest wind speed class (dashed line), where behavior of individual nights may affect the composite significantly; see Table 1]. After sunset, the composite heat flux strongly depends on the wind speed class. For weakly stable cases (blue) a temporal maximum downward heat flux (not to be confused with the maximum of Fig. 1) is visible just after sunset. This typical behavior is beyond the scope of this study. Later ($t \geq 3\,\mathrm{h}$) a more or less steady value is reached. In the very stable cases (red) the maximum is much less pronounced owing to the fact that turbulence is strongly suppressed (Fig. 3). Later on the flux reaches a more or less constant, ''preferred'' value of $|H_0| \approx 10.0 \pm 3.5\,\mathrm{W\,m^{-2}}$.

d. Temperature inversion characteristics

In Fig. 5 the temperature inversion is given as a function of wind speed at a reference level z ($z = 10$, 20, 40, or 80 m). The inversion is defined as the difference in (potential) temperature between the reference level and 1. 5 m above the surface: $\Delta\theta = \theta(z) - \theta(1.5\,\mathrm{m})$. In the same figure time evolution is given by the ''brightness'' of the colors: an increment in shade indicates a 10-min advance.

For each altitude, we observe that $\Delta\theta$, for each wind speed class, approaches a well-defined line in the diagram within the first few hours. At the low–wind speed side, these lines are significantly steeper than at the high–wind speed side. It is found that an initial U_{40} of $5.5\,\mathrm{m\,s^{-1}}$ separates the steep branch from the slightly oblique branch at each level. As such, the division in colors at $U_{40} = 5.5\,\mathrm{m\,s^{-1}}$ is applied to all figures in the present paper.

For the very stable cases (red), clearly the effect of flow acceleration is visible. Because the dots of several classes overlap, the black arrow is inserted to illustrate the

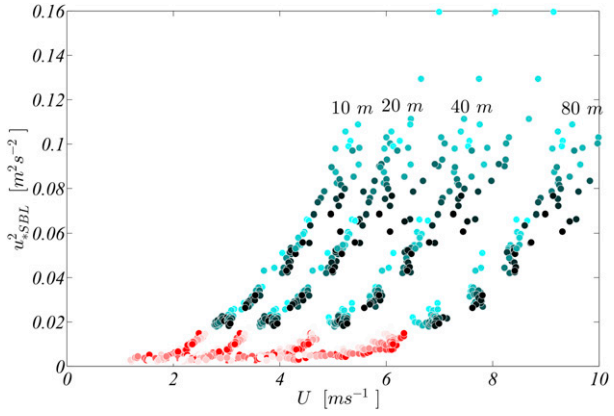

FIG. 6. The near-surface kinematic stress is shown as a function of the wind speed for $z = 10, 20, 40$, and 80 m. Color coding is as in Fig. 5. Note that a different time frame is used here. The shades indicate times between $t = 1$ (lightest shade) and $t = 3$ h (darkest shade).

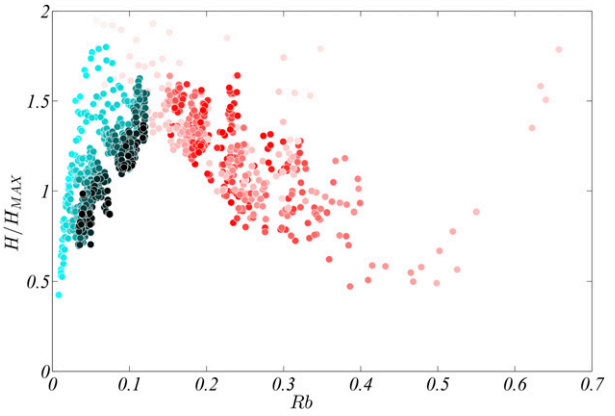

FIG. 7. The scaled turbulent heat flux as function of the bulk Richardson number is shown (defined in the text) for $z = 40$ m. The maximum of the curve appears to coincide with the abrupt change of slope in Fig. 5. Color coding and time frame are as in Fig. 5.

temporal development for the case $U_{40} \in [1.0; 1.5]\,\mathrm{m\,s^{-1}}$ (Table 1): an initial increase in $\Delta\theta$ is followed by a decrease (flow acceleration causes more turbulent mixing), until finally, like before, a preferred state is reached. For example, at 40 m the end state for all very stable cases lies around $[U, \Delta\theta] \approx [4.3\,\mathrm{m\,s^{-1}}, 2.5\,\mathrm{K}]$. In contrast, weakly stable cases rapidly reach their specific end state.

e. The minimum wind speed

Contrary to the inversion strength, turbulent stress is observed at a single level (before and after September 2006: 5 and 3 m, respectively). Figure 6 shows the turbulent stress as a function of the wind speed at a reference height (again $z = 10, 20, 40$, and 80 m) for the initial stage of the night.

Figure 6 shows a characteristic shape, which is consistent with the on–off behavior of nocturnal turbulence: below a certain threshold value, steady turbulence cannot be sustained (cf. VDW12a). At the same time, the authors realize that truly on–off behavior is unlikely to occur in nature. Here, in the observations, on–off behavior is smoothed by secondary dynamics and by the averaging procedure itself. Apart from this caveat, as the wind speed increases with height, different observational levels indicate different critical values. Note that similar dependencies have already been reported in observations by King et al. (1994) and Sun et al. (2012). However, the critical case occurs simultaneously throughout the boundary layer: it occurs when the wind speed class (Table 1) drops below $5.5\,\mathrm{m\,s^{-1}}$ (at the 40-m level). The similarity in shapes and the coincidence of the critical wind speed class invite us to use the critical wind speed value for normalization of the horizontal axis. Later, the theoretical concept of the minimum (critical) wind speed is used for this purpose.

f. The maximum sustainable heat flux

The effects of wind speed and temperature are combined in a nondimensional graph that depicts the turbulent heat flux as a function of the bulk Richardson number (Fig. 7). Here, the bulk Richardson number is defined as $R_b = (g/\theta_0)(z\Delta\theta/U^2)$ (in Fig. 7, $z = 40$ m). For normalization of the turbulent heat flux the so-called maximum sustainable heat flux $|H_{\max}|$ is used (VDW12b):

$$|H_{\max}| = \frac{4}{27\alpha}\frac{\kappa^2 \rho c_p \theta_0}{g}\frac{U^3}{z[\ln(z/z_0)]^2}, \qquad (1)$$

where κ is the von Kármán constant (0.4), α is a closure parameter for log-linear flux-profile relations (set to $\alpha = 4$, based on current observations), ρ is the density of air ($1.2\,\mathrm{kg\,m^{-3}}$), c_p is the heat capacity of the air at constant pressure ($1005\,\mathrm{J\,kg^{-1}\,K^{-1}}$), θ_0 is the typical air temperature (285 K), g is the gravitational constant ($9.81\,\mathrm{m\,s^{-2}}$), z_0 is the local surface roughness length (0.03 m; Bosveld 2014), z is the height above the surface, and $U(z)$ is the wind speed at z.

The derivation of this expression is summarized in the next section. Note that the scaling itself is general, whereas the (optional) prefactor $[4/(27\alpha)]$ arises from specific model assumptions (here, the validity of log-linear Businger–Dyer similarity functions; see below). From Fig. 7 (cf. the dimensional sketch in Fig. 1), it appears that the turbulent heat flux maximizes at intermediate stability. This effect has been well known in literature (e.g., Mahrt et al. 1998; Grachev et al. 2005;

Sorbjan 2006). Physically, it reflects the fact that the heat flux is limited in its neutral extreme (absence of vertical temperature gradients) and in its very stable extreme (suppressed vertical mixing). Interestingly, the maximum coincides with the regime separation [see also Mahrt et al. (1998)] proposed in Fig. 5. Note that formal analysis on a simplified, plate-driven Couette flow showed that at this maximum a negative feedback in the heat transport suddenly changes into a positive feedback, which eventually causes a regime shift to occur (van de Wiel et al. 2007). At other altitudes (10, 20, and 80 m; not shown), the regime (color) separation also occurs at the maximum heat flux, albeit at different bulk Richardson numbers. This aspect is discussed later.

Note that direct interpretation of Fig. 7 in terms of Fig. 1 is nontrivial: The vertical axis of Fig. 7 is normalized with $H_{\max}$; as such, each class is scaled with a different value. Idealistically (in theory) the turbulent heat flux curves would coincide (cf. van de Wiel et al. 2007). Figure 1, alternatively, is normalized with a single value of the energy demand set by the net radiation.

With respect to the time dependence (color intensity), the weakly stable (blue) cases approach a steady state within 3 h (conglomerates of black points), whereas the very stable cases show a systematic variation during the night: the aforementioned acceleration causes a decrease in the bulk Richardson number ($R_b \sim 1/U^2$) until again some kind of preferred state is reached at $R_b \approx 0.2$. Note that as bulk quantities at a single altitude are considered, the generality of this number must be taken with caution. At first impression, the observation of this preferred state might point to the conjecture made by Wang and Bras (2010). They state that the MO similarity functions have a single solution. However, this is not the case, as their claim of such state being the only possible state cannot be justified: weakly stable cases can have any stability between neutral and $R_b \approx 0.2$.

4. Shear capacity as regime prognostic

Figures 5 and 6 show that the value of the critical wind speed depends on the observational height. On the other hand, it is clear that the regime transition of the boundary layer as a whole cannot depend on a specific observational height. In VDW12b instead, it is shown that a transition is expected when the radiative heat loss at the surface is significantly larger than the maximum downward turbulent heat flux that can be supported by the flow at a given wind profile. Vice versa, one may start from the assumption that the maximum sustainable heat flux should attain a significant fraction of the net radiative heat loss (say an arbitrarily chosen fraction of approximately 25% or about 10 W m^{-2}) to prevent extreme cooling (and hence the collapse of turbulence). To obtain the expression for the critical profile, we follow VDW12a. We start with the surface energy balance, which is written as

$$c_v \frac{\partial T_s}{\partial t} = |H_0| - (|Q_N| - |G|). \tag{2}$$

For convenience, we use the absolute values of the fluxes here; as such, positive fluxes are directed toward the surface. We consider a case just after sunset for an isolating surface with low heat capacity per unit area c_v (J m^{-2} K^{-1}) like fresh snow or short grass. The key question is whether, at a given wind profile, sufficient heat can be transported such that $|H_0| \gtrsim O(|Q_N| - |G|)$ to prevent extreme surface cooling.

To describe the turbulent heat flux as a function of temperature and wind speed, we adopt MO similarity (Monin and Obukhov 1954) using bulk quantities. Though this is a crude assumption, it was shown by VDW12a that the final result is not very sensitive to this approximation and that formal local similarity, allowing for effects of flux divergence, leads to qualitatively similar answers (appendix A). The turbulent heat flux is modeled via (e.g., Louis 1979; McNider et al. 1995)

$$|H| = \frac{\rho c_p \kappa^2}{[\ln(z/z_0)]^2} U \Delta\theta f(\alpha R_b), \tag{3}$$

with $R_b = z(g/\theta_0)(\Delta\theta/U^2)$ (other quantities are defined as in the previous section). For $f(\alpha R_b)$, we take

$$\begin{aligned} f(\alpha R_b) &= (1 - \alpha R_b)^2; \quad R_b \le 1/\alpha, \\ f(\alpha R_b) &= 0; \quad R_b \ge 1/\alpha. \end{aligned} \tag{4}$$

This is equivalent to assuming log-linear similarity functions $\phi_{m,h} = 1 + \alpha z/L$ (e.g., McNider et al. 1995; King and Connolley 1997). Next, rearrangement leads to

$$|H| \frac{g}{\theta_0} \frac{\alpha z [\ln(z/z_0)]^2}{\rho c_p \kappa^2 U^3} = \alpha R_b (1 - \alpha R_b)^2 \quad \text{for} \quad R_b \le 1/\alpha. \tag{5}$$

By differentiating Eq. (5) with respect to αR_b, an expression for the maximum achievable heat flux is obtained. The maximum is reached at $\alpha R_b = 1/3$ (e.g., Taylor 1971; Malhi 1995; Basu et al. 2008) and reads (in dimensional terms)

$$|H_{\max}| = \left(\frac{4}{27\alpha}\right) \frac{\rho c_p \theta_0 \kappa^2}{g} \frac{U^3}{z \ln(z/z_0)^2}. \tag{6}$$

Note that the prefactor on the rhs (in parentheses) depends on the assumed specific closure $f(\alpha R_b)$. In line with the discussion above, we require that the maximum achievable heat flux should be above the demand $|Q_N| - |G|$ at the surface. By substituting $|Q_N| - |G|$ for $|H_{\max}|$ in Eq. (6), we find the minimum wind speed profile for sustained turbulence:

$$U_{\min} = \left(\frac{27\alpha}{4}\right)^{1/3} \left\{ \frac{g}{\theta_0 \kappa^2} \frac{(|Q_N| - |G|)}{\rho c_p} z[\ln(z/z_0)]^2 \right\}^{1/3}. \quad (7)$$

This then corresponds to a critical wind profile—that is, the minimum wind profile needed to sustain turbulence in the boundary layer as a whole. The horizontal axis of Fig. 6 is normalized using this critical profile to arrive at Fig. 8. From the color separation in this figure, it appears that indeed the regime transition can be predicted irrespective of the specific observational height.

Next, an estimate for the heat flux demand $|Q_N| - |G|$ at the surface is needed. From Fig. 4, at least some $10\,\mathrm{W\,m^{-2}}$ has to be supported by the heat flux in order to sustain turbulence (either blue cases or red cases at the end of the night). Therefore, we take this value as an estimate for the demand in Eq. (7). Note, that because of the 1/3 exponent in the $U_{\min}$ formulation the dependence to the exact value is weak. Moreover, it will be shown that the regime separation itself is independent of the specific demand, provided that a fixed value is taken.

We now propose to normalize the wind speed with the minimum wind speed $U/U_{\min}$. This means that one compares the actual shear with the minimum shear needed to sustain a downward heat flux of significant magnitude.

As log-linear similarity functions are used in the derivation, clearly Eq. (7) is a specific result for that choice. However, adopting other similarity functions would result in the same equation for $U_{\min}$ with the exception that the prefactor [in this case $(27\alpha)/4$] would be different but still a constant. Thus, the fact that the regimes in Fig. 8 separate is not affected by a particular choice for the closure.

It occurs that the aforementioned transition points coincide into a single critical point: the normalization separates weakly stable from very stable cases irrespective of the specific observational height. Hence, a single wind speed observation suffices to predict the state of the clear nocturnal boundary layer just after sunset. This is the desired result. In the example above, the critical value lies at $U/U_{\min} = 1.04$. Here, via $U_{\min}$ the critical value itself depends on our closure model and choice $|Q_N| - |G| = 10\,\mathrm{W\,m^{-2}}$. Alternatively, one could eliminate those choices from the normalization procedure and replace the demand directly by a fixed value of $|Q_N|$ "representative" for clear skies (see section 5). Although this would change the critical value, it clearly does not affect the separation itself.

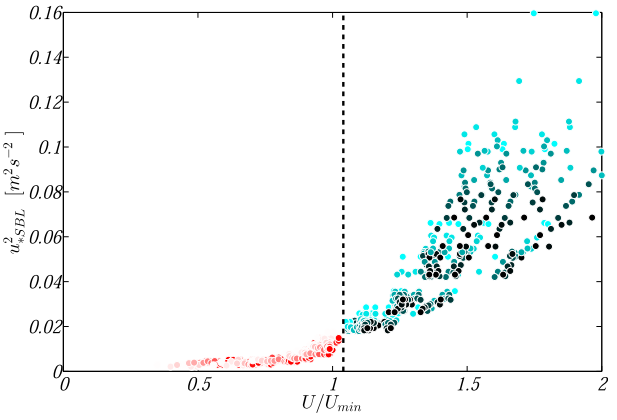

FIG. 8. The kinematic stress as function of the normalized wind speed [using Eq. (7)] is shown for $z = 10$, 20, 40, and 80 m. Color coding is as in Fig. 5. Note that a different time frame is used here. The shades indicate times between $t = 1$ (lightest shade) and $t = 3$ h (darkest shade). Normalization of the horizontal axis results in a unique separation irrespective of the observational height.

Here, we would like to discuss the normalization procedure apart from any specific $f(R_b)$ closure. Because $U/U_{\min}$ compares the actual shear with the minimum required, we coin a new closure-independent parameter as the SC. In bulk properties, it is defined as

$$\mathrm{SC} = U \left\{ \frac{g}{\theta_0 \kappa^2} \frac{|Q_N| - |G|}{\rho c_p} z[\ln(z/z_0)]^2 \right\}^{-1/3}, \quad (8)$$

whereas in gradient terms it reads as (see also section 5)

$$\mathrm{SC} = \frac{(\partial U/\partial z)}{(\partial U/\partial z)_{\min}} = \left(\frac{\partial U}{\partial z}\right) \left(\frac{g}{\theta_0 \kappa^2} \frac{|Q_N| - |G|}{\rho c_p} \frac{1}{z^2} \right)^{-1/3}. \quad (9)$$

Note that in Fig. 8: $U/U_{\min} = [4/(27\alpha)]^{1/3}\mathrm{SC}$, using the bulk form. In the remainder of the text, the model-independent SC is used instead of $U/U_{\min}$ to predict regime transition.

Ambiguity of local stability indicators

In atmospheric literature, z/L or R_i are successfully used to indicate local atmospheric stability at a specific altitude above the surface. At the same time, it can be anticipated that those local stability indicators cannot provide direct information on the global state of the boundary layer (being weakly or very stable).

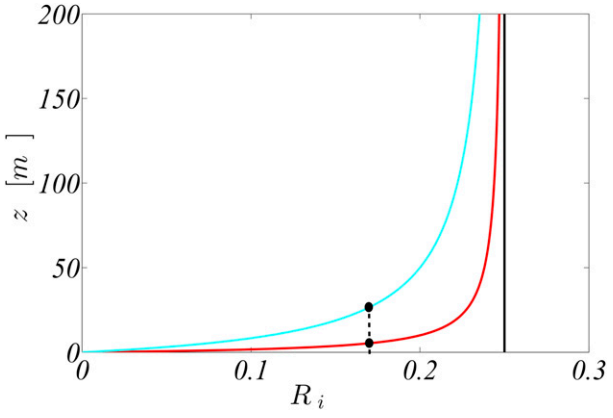

FIG. 9. Theoretical profiles of the Richardson number based on Monin–Obukhov theory for $L = 10$ (red) and $L = 50$ m (blue). The dots illustrate the fact that a single value of R_i (here 0.17) does not unambiguously relate to one regime.

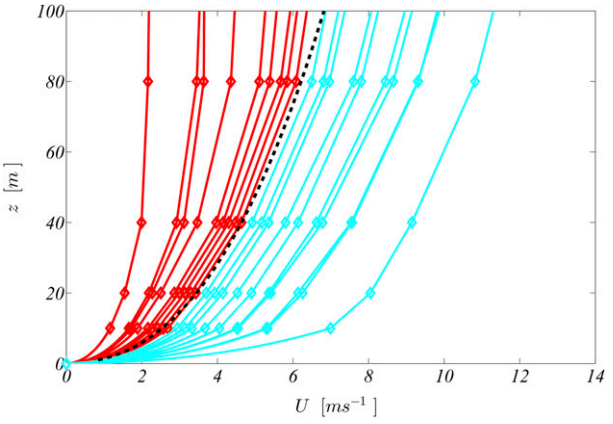

FIG. 10. Wind profiles at $t = 1$ h: very stable (red) and weakly stable (blue) and the theoretical minimum wind speed based on Eq. (7) (black). Note that above $z = 100$ m the theory is not valid. The 10-m data points are interpolated log linearly to the surface for visualization purposes.

To illustrate this, we analyze two cases: a "weakly stable" boundary layer with an Obukhov length $L = 50$ m and a "very stable" regime with $L = 10$ m. Under MO theory,

$$\phi_m = \frac{\partial U}{\partial z}\frac{\kappa z}{u_*} \quad \text{and}$$
$$\phi_h = \frac{\partial \theta}{\partial z}\frac{\kappa z u_* \rho c_p}{|H|}, \tag{10}$$

so $R_i = (z/L)\phi_h/\phi_m^2$. As before, we take $\phi_{m,h} = 1 + \alpha z/L$ (for $\alpha = 4$), so that $R_i = z/L(1 + \alpha z/L)^{-1}$. Figure 9 shows the corresponding profiles of the gradient Richardson number. It is clear that a specific R_i (e.g., $R_i = 0.17$) corresponds to two completely different situations (black dots): either the boundary layer is very stable and shallow and R_i was monitored at a low observational level or the boundary layer is deeper and in a more turbulent state, but monitoring was done at a higher altitude. As such, we cannot unambiguously describe the state of the atmosphere by a Richardson number alone.

A similar ambiguity arises when z/L is used. This parameter can both change because of changing flux conditions or because of a different observation height. As such, a regime division based on the value of z/L solely—for example, such as presented in Mahrt et al. (1998)—cannot be unique.

Wind speed profiles at $t = 1$ h are depicted in Fig. 10. The thick black dashed line is the minimum wind speed profile [Eq. (7)]. We observe that at $t = 1$ h the wind speed is weaker than the minimum profile in all very stable cases (presunset $U_{40} < 5.5\,\mathrm{m\,s^{-1}}$, red) and stronger in all weakly stable cases ($U_{40} > 5.5\,\mathrm{m\,s^{-1}}$, blue). Of course, later during the night the air in the very stable cases accelerates (e.g., Fig. 2) so that $U(z) \approx U_{\min}(z)$ and turbulence is recovered. Figure 10 illustrates that the shear capacity largely eliminates this ambiguous height dependence and is therefore more useful as a global regime indicator for the wind profiles just after sunset.

The difference between z/L and R_b (as proxy for R_i) versus SC becomes clear by analysis of the observational data with respect to u_*^2 as a function of the stability parameter (Figs. 11a,c,e). Both z/L and R_b show a region of intermediate stability where the regime is not uniquely defined. Note that normalization of the vertical axis is omitted here as for the main observational period local flux information above $z = 5$ m is not available. Clearly, the regime separation in Figs. 11e and 11f does not depend on a specific observation level. A similar result is obtained when the temperature inversion strength is analyzed (Figs. 11b,d,f). Note, that even in this nonscaled form Figs. 11a–c are strongly influenced by self-correlation (Klipp and Mahrt 2004; Baas et al. 2006). If, for example, the horizontal and vertical axes of Fig. 11c are compared, we see that $z/L \sim u_*^{-3}$, while the vertical axis also contains u_*. As such, the observed relation between z/L and u_*^2 is not necessarily physical.

5. Physical interpretation

In our analysis, the criterion for regime transition depends on whether energy loss (demand) at the surface can be compensated under a given wind profile. This comparison is expressed in a nondimensional parameter: SC [Eq. (9)]. In this section, we evaluate the idealized, academic case, such that a fixed heat flux can be imposed.

The following strategy is used: First, we use the turbulent kinetic energy (TKE) budget to show that we can expect the shear capacity and momentum flux to be

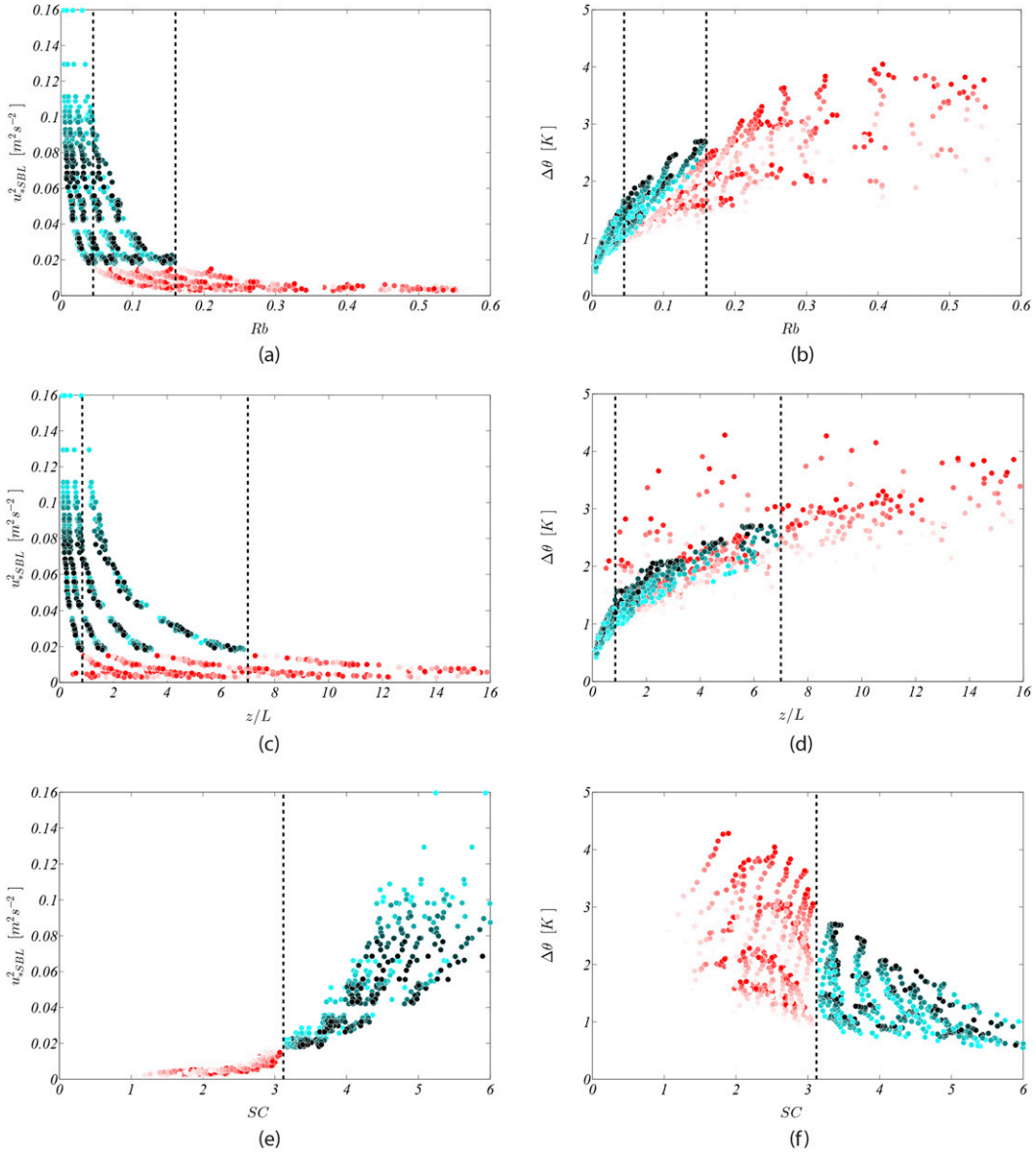

FIG. 11. The stability indicators are compared: (a) R_b vs u_*^2, (b) R_b vs $\Delta\theta$, (c) z/L vs u_*^2, (d) z/L vs $\Delta\theta$, (e) SC vs u_*^2, and (f) SC vs $\Delta\theta$. SC is as defined in Eq. (8). The dashed lines indicate the region of regime transition. Clearly the regimes are only separated independently of the observational height when the horizontal axis is normalized with the minimum wind speed. Color coding is as in Fig. 5. Note that a different time frame is used here. The shades indicate times between $t = 1$ (lightest shade) and $t = 3$ h (darkest shade).

uniquely related. Then, the generic relation (with the constraint that MO theory is valid) between shear capacity and momentum flux is obtained, using traditional MO theory. This results in the nondimensional counterpart of Fig. 8. The theoretical relation is compared to field observations. Finally, the current analysis is put into perspective of local scaling theory.

This case is set up as follows: According to Fig. 1 flow transition is driven by a heat flux demand $|H_0|$ at the surface. As such, we prescribe a constant heat flux equal to a significant fraction of the net radiation: $|H_0| = c|Q_N|$, with c a fraction on the order of 0.1–1. Although reality is much more complex, one could think of this case representing a stable boundary layer over a surface, covered with fresh snow just after sunset (such that the soil heat flux is small). Note that in numerical simulations such a flux-driven case is easily set up (Jiménez and Cuxart 2005; Nieuwstadt 2005). Furthermore, we assume wind (shear) to be fixed such that flow-acceleration effects have not yet occurred at the boundary.

a. Relation between shear capacity and dimensionless shear

Below, we evaluate how the surface constraint $|H| = |H_0| = c|Q_N|$ translates into the TKE budget of the flow near the surface. With $|H| = |H_0|$, the steady TKE budget reads (ignoring transport terms)

$$0 = \frac{\partial e}{\partial t} = -\overline{u'w'}\frac{\partial U}{\partial z} - \frac{g}{\theta_0}\frac{|H_0|}{\rho c_p} - \epsilon. \tag{11}$$

Next, we divide the equation by $(\kappa z)^2(\partial U/\partial z)^3$ and obtain

$$0 = \frac{-\overline{u'w'}}{(\kappa z)^2(\partial U/\partial z)^2} - \frac{(g/\theta_0)(|H_0|/\rho c_p)}{(\kappa z)^2(\partial U/\partial z)^3} - \frac{\epsilon}{(\kappa z)^2(\partial U/\partial z)^3}. \tag{12}$$

This dimensionless equation can be recognized as

$$0 = \phi_m^{-2} - \frac{1}{\mathrm{SC}^3} - \hat{\epsilon}, \tag{13}$$

with ϕ_m^{-2} the dimensionless flux [Eq. (10)] and $\hat{\epsilon}$ the dimensionless dissipation.

In this flux-driven system, we expect that ϕ_m and SC are uniquely related (dissipation is merely determined by the other terms, which act at the generating scales). SC is determined by two external parameters: H_0 and $\partial U/\partial z$. For a given value of $\partial U/\partial z$, one can predict this relation $\phi_m(\mathrm{SC})$ using traditional MO relations by taking $H = H_0$ (a derivation is provided in appendix B):

$$\mathrm{SC}^{-3} = R_i f_h(R_i) \quad \text{and}$$
$$\phi_m^{-2} = f_m(R_i). \tag{14}$$

With these relations, the traditional flux-profile relations can be mapped exactly to an alternative scaling based on the shear capacity, provided the following requirements are met:

- steady state is reached,
- $f_{m,h}$ are known, and
- $|H_0|$ is prescribed at the surface.

For the simplest, linear, flux-profile relations, Eqs. (14) can be solved analytically (using $f_{m,h} = 1 - 8R_b$; to compare with data later, we switch back to the bulk formulation). This results in (see appendix B)

$$\phi_m^{-2} = \frac{1}{2}(1 + \sqrt{1 - 32\mathrm{SC}^{-3}}). \tag{15}$$

This solution is shown in Fig. 12 (solid line). For more complex flux-profile relations, Eqs. (14) have to be solved numerically. The dashed–dotted line shows the

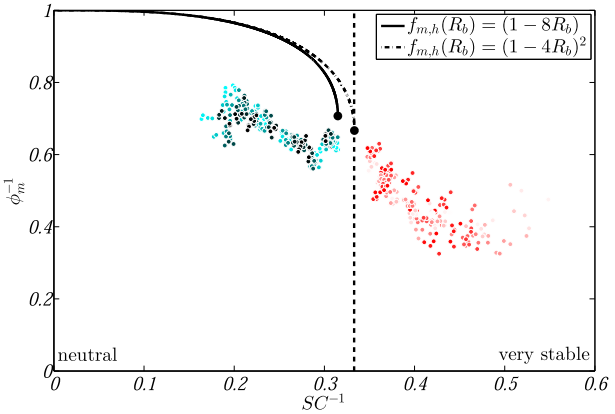

FIG. 12. Equations (14) are solved for several choices for the similarity functions (see legend). This results in the two black lines, which show the steady-state solution of the dimensionless shear as a function of the shear capacity. Beyond the endpoint of the lines, no (steady) solution is possible as it requires $H > H_{\max}$ (cf. Fig. 1). Field observations are collected at the 20-m level. Note that for this figure a different time frame is used. The shades indicate times between $t = 2$ (lightest shade) and $t = 6$ h (darkest shade). Here, later times are chosen to focus on the steady state of the weakly stable cases.

numerical solution to Eqs. (14) using the more complex Businger–Dyer relations [$f_{m,h} = (1 - 4R_b)^2$]. Note that Fig. 12 shows SC^{-1} on the horizontal axis; thus, stability increases to the right. The endpoint (thick black dot) of each line corresponds to the critical point, where Eqs. (14) yield no solution for smaller SC. Physically, this corresponds to the point where wind shear is too low (SC^{-1} is too large) such that $|H_0|$ cannot be supported by the flow.

Note that as our regime transition is driven by the surface energy budget, rather than by the flow alone, our analysis is not in disagreement with, for example, Galperin et al. (2007) and Zilitinkevich et al. (2008), who state that such transition cannot be predicted by merely considering the TKE budget. Here, through coupling of flow and boundary conditions, a sudden collapse, or rather a qualitative regime transition, of turbulence can be predicted. It is unlikely, however, that such a collapse leads to complete laminarization in real atmospheric flows as motivated in Mauritsen et al. (2007) and Zilitinkevich et al. (2008).

Ideally, a comparison with field observations would be made for a range of values of SC^{-1}. Field observations in general, however, do not meet the requirements as formulated above. As such, we cannot make a fair comparison between the field observations and the theoretical prediction. Especially flux divergence and the fact that $|H_0|$ is not fixed account for the significant deviation of the data points (colored dots in Fig. 12) from the theoretical prediction. The transition point itself, however, is weakly sensitive to the prescribed $|H_0|$. This is expressed in the fact that the regime separation (vertical dashed line) is predicted accurately by the

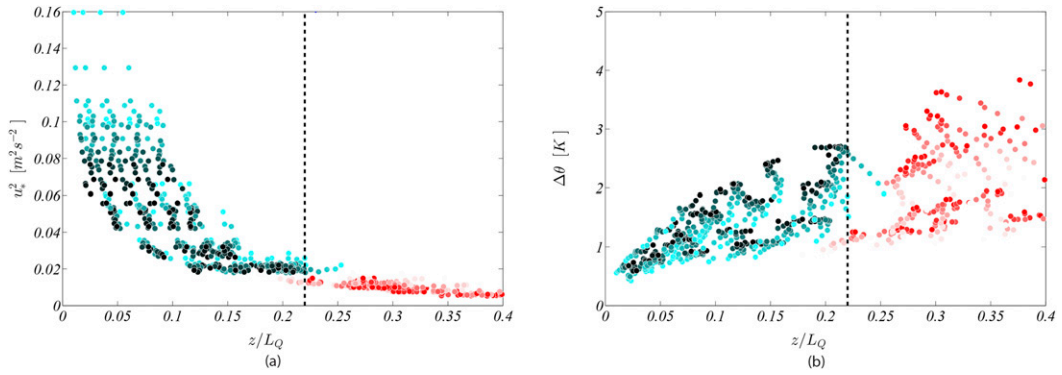

FIG. 13. The near-surface kinematic stress vs the Monin–Obukhov stability parameter for a fixed energy demand. Here the Obukhov length is defined as in Eq. (18) with $cQ_N = 10\,\mathrm{W\,m^{-2}}$. Color coding is as in Fig. 5. Measurements at levels 10, 20, 40, and 80 m. The regimes are separated fairly well by the parameter z/L_Q. Note that a dominant self-correlation occurs in (a).

Businger–Dyer relations. In a controlled experiment (e.g., Nieuwstadt 2005) such a case as in Fig. 12 could be realized. Therefore, these cases will be analyzed in a separate study. From a field-observations perspective, agreement is only expected when the measurements (including flux profiles) are conducted over a strongly insulated surface (e.g., a snow-covered plane).

Note that a similar analysis can be made in order to arrive at a dimensionless equivalent to the inversion strength $\Delta\theta$ of Fig. 5. In gradient terms, this results in a relation (see also appendix B):

$$\frac{g}{\theta_0}\frac{\partial\theta}{\partial z}\left(\frac{\theta_0\kappa^2\rho c_p z^2}{g|H_0|}\right)^{2/3} = f(\mathrm{SC}). \tag{16}$$

However, here we limit ourselves to the proof-of-principle case above.

Considerations on the possibility of self-correlation reveal that, for this case, strong self-correlation would imply a linearly increasing relation between SC^{-1} ($\sim U^{-1}$) and ϕ_m^{-1} ($\sim U^{-1}$). However, the anticipated physical relation in Fig. 12 is a decreasing one. As such, the self-correlation is not expected to play a large role here.

b. Local scaling

Finally, an interesting viewpoint is obtained by reconsidering the surface-driven TKE budget [Eq. (11)] and multiplying it by the MO scaling term $\kappa z/u_*^3$, which results in

$$0 = \phi_m - z/L_Q - \tilde{\epsilon}, \tag{17}$$

with $\tilde{\epsilon}$ the dimensionless dissipation and

$$z/L_Q = \frac{\kappa z g}{\theta_0 \rho c_p}\frac{|cQ_N|}{u_*^3}. \tag{18}$$

Here, L_Q represents an "Obukhov length" based on a fixed surface flux $|cQ_N| = |H_0| = 10\,\mathrm{W\,m^{-2}}$. Physically speaking, the concept of L_Q is of little value as the traditional definition of L was formulated and interpreted in terms of observed $|H|$. Mathematically, however, the relation above is similar to Eq. (13). This implies that z/L_Q is expected to separate the regimes as was the case with SC. Figure 13 shows that this is indeed the case (cf. Figs. 11c and 11d).

The reason for this surprising result lies in the fact that z/L_Q compares the surface energy demand to the maximum heat flux under given shear—similar to SC (see discussion).

6. Discussion

In this section, we briefly discuss usage of the shear capacity in relation to local stability indicators such as R_i and z/L.

As the atmospheric boundary layer is relatively well mixed during the day, fluxes are large compared to gradients. This inspired flux-based scaling in the form of the Obukhov length (z/L) (Monin and Obukhov 1954). In contrast, turbulence is much weaker during nighttime (e.g., Stull 2000). In this case, gradients are relatively large compared to fluxes. This leads to gradient-based scaling using the gradient Richardson number (Sorbjan 2006). A similar advantage occurs for the shear capacity, where both U and $U_{\min}$ are of significant magnitude in the VSBL regime. Although the amount of observational scatter may depend on whether fluxes or gradients are used, in principle, the same flux-gradient relation will result. Mathematically speaking, a relation in terms of $\phi_m(z/L)$ can therefore be converted into $f_m(R_i)$ and vice versa [as discussed in van de Wiel et al. (2008)]. Both methods suffice in order to relate the local gradients to the local fluxes to form a consistent closure model. On the

other hand, both z/L and R_i are height-dependent parameters so that their value is nonuniquely related to a single boundary layer regime.

In the present study, a nontrivial mix of flux and gradient is used. The energy demand of $|H_0|$ is used as a flux parameter. It is on the order of the net radiative heat loss and hence usually not small in cases when regime transitions are expected. The fact that none of the scaling parameters become small in the very stable regime explains the surprisingly low amount of scatter of the red points in, for example, Fig. 8. Additionally, wind shear is an important variable as it drives the production of turbulence during the night (Sun et al. 2012). Both variables are combined in the nondimensional shear capacity, which relates the flow to the boundary condition. As before, it is shown that the value of this parameter uniquely relates to the occurrence of boundary layer regimes.

We symbolically summarize the scaling alternatives as

1) scaling with internal flow parameters, flux-gradient relations

$$[u_*; H; \kappa z] \rightarrow z/L, \quad [\partial U/\partial z, \partial\theta/\partial z] \rightarrow R_i, \quad \text{and}$$

2) scaling with flow parameters and boundary conditions of imposed flux, prediction of regime transition

$$[\partial U/\partial z; H_0; \kappa z] \rightarrow \text{SC}.$$

7. Conclusions

In this work, an ensemble averaging procedure is applied to field observations. This allows the study of typical behavior of clear nights in classes of similar wind forcing. We emphasize that in the present study strong assumptions had to be made in the application of Monin–Obukhov similarity theory beyond its formal range of validity. For an analysis on this important issue, we therefore refer to Sun et al. (2012). To the observations, surface-based scaling is applied up to an altitude of 80 m. In general, effects such as flux divergence can no longer be ignored at such altitudes. Still, in this case, the observations regarding a regime transition appear not to deviate from predictions based on the surface-layer theory. From the analysis, we can conclude the following:

1) For the boundary layer as a whole, two qualitatively different regimes exist in the initial stage of the night: a weak wind case that is nonsteady and characterized by weak turbulence and a strong temperature inversion. The strong wind case on the other hand is steady and characterized by continuous, relatively strong turbulence and a limited temperature inversion.
2) The regime can be unambiguously indicated by the introduction of a new dimensionless group: the shear capacity of the flow. This group compares the required wind shear (based on the required surface heat flux) and the actual wind shear.

Analysis of the temporal development reveals that "collapsed" cases tend to recover to a more turbulent state later at night. This state appears to be rather similar among all very stable cases.

Finally, a theoretical analysis is made as well. This results in nondimensional relations between the momentum flux and shear capacity. In the future this scaling behavior of the shear capacity will be investigated in more idealized environment using direct numerical simulation (DNS) [e.g., as in Nieuwstadt (2005), Flores and Riley (2011), and Ansorge and Mellado (2014)]. This allows in-depth analysis of the proposed nondimensional physical relationships.

Acknowledgments. We are thankful to the many fruitful discussions which took place at NCAR during the sabbatical leave of the last author at this institute during the summer of 2013. In particular, this author thanks Jielun Sun, Pete Sullivan, Ned Patton, Chin-Hoh Moeng, Peggy Lemone, and Jeff Weil for their specific suggestions on the topic. Additionally, recent discussions on related work with Arnold Moene, Harm Jonker, and Peter Baas are highly appreciated. Finally, the research has been supported by a VIDI Grant (10011425) and an ALW Grant (82301010) from the Dutch National Science Foundation (NWO), which is gratefully acknowledged.

APPENDIX A

Maximum Sustainable Heat Flux

Analog to the bulk approach in section 4, a gradient approach can be followed. In gradient terms the heat flux reads

$$\frac{|H|}{\rho c_p} = (\kappa z)^2 \frac{\partial U}{\partial z}\frac{\partial \theta}{\partial z} f(\alpha R_i). \tag{A1}$$

Normalization yields

$$|\widehat{H}| = \frac{|H|}{\rho c_p}\frac{\alpha g}{\theta_0 (\kappa z)^2 (\partial U/\partial z)^3} = \alpha R_i f(\alpha R_i). \tag{A2}$$

Setting the derivative with respect to αR_i equal to zero gives a value for αR_i at which the maximum heat flux can be attained. In the case of the log-linear closure this yields $|\widehat{H}|_{\max} = 4/27$. Returning to the dimensional

equation for $|H|$, we observe that the dimensional maximum sustainable heat flux $|H_{\max}| \approx (\partial U/\partial z)^3$.

APPENDIX B

Relation between ϕ_m and SC

Here, a short derivation is provided for the shear capacity in terms of the bulk Richardson number (conversion to the gradient case is straightforward). The same academic case as in section 5 is used; that is, we assume $|H| = |H_0|$ is known, the shapes of the flux-profile relations are known, and a steady state is reached. Next, an example is given of a case in which the conversion from the flux-profile relations to the shear capacity formulation can be made analytically.

In bulk formulations the turbulent heat flux reads

$$\frac{H_0}{\rho c_p} = \frac{\kappa^2}{[\ln(z/z_0)]^2}\Delta U \Delta\theta f_h(R_b). \tag{B1}$$

Multiplication with $\{gz[\ln(z/z_0)]^2\}/(\theta_0\kappa^2\Delta U^3)$ yields

$$\mathrm{SC}^{-3} = \frac{gz[\ln(z/z_0)]^2 H_0}{\theta_0 \rho c_p \kappa^2 \Delta U^3} = R_b f_h(R_b). \tag{B2}$$

Similarly, the bulk formulation of the kinematic stress

$$u_*^2 = \frac{\Delta U^2 \kappa^2}{[\ln(z/z_0)]^2} f_m(R_b) \tag{B3}$$

can be rewritten to the normalized momentum flux:

$$\phi_m^{-2} = \frac{u_*^2[\ln(z/z_0)]^2}{\Delta U^2 \kappa^2} = f_m(R_b). \tag{B4}$$

These results are used in Eq. (14) of the main text and in the example below.

Example case: Analytical conversion

This example aims to provide insight in the mathematical conversion from the flux-profile relations to the SC formulation. To show the principal steps, linear flux-profile relations are used, as the Businger–Dyer relations would yield an intractable derivation.

The linear profiles are entered into Eq. (B2):

$$\mathrm{SC}^{-3} = R_b \max\{(1 - 8R_b), 0\}. \tag{B5}$$

This quadric equation is solved for R_b (only the physical solution is presented):

$$R_b = \frac{1}{16}(1 - \sqrt{1 - 32\mathrm{SC}^{-3}}). \tag{B6}$$

This result is then substituted in Eq. (B4):

$$\phi_m^{-2} = \frac{1}{2}(1 + \sqrt{1 - 32\mathrm{SC}^{-3}}). \tag{B7}$$

By differentiating Eq. (B5) with respect to R_b, the critical value for SC^{-3} is obtained (i.e., $\mathrm{SC}^{-3} = 1/32$). This is also expressed in the fact that Eq. (B7) becomes invalid for $\mathrm{SC}^{-1/3} > 1/32$. Thus, the critical point is $\{\mathrm{SC}_c^{-1}, \phi_{m,c}^{-1}\} = \{\sqrt[3]{1/32}, 1/\sqrt{2}\}$ (thick black dot in Fig. 12).

The normalized temperature difference is derived in a similar fashion:

$$\widehat{\Delta\theta} = \frac{g}{\theta_0} z\Delta\theta \left\{\frac{\theta_0\kappa^2\rho c_p}{g|H_0|z[\ln(z/z_0)]^2}\right\}^{2/3}$$
$$= \mathrm{SC}^2 R_b = \frac{\mathrm{SC}^2}{16}(1 - \sqrt{1 - 32\mathrm{SC}^{-3}}). \tag{B8}$$

REFERENCES

Acevedo, O., and D. Fitzjarrald, 2000: Relating temporal and spatial structure of the nocturnal surface layer to landscape heterogeneity. *14th Symp. on Boundary Layer and Turbulence,* Aspen, CO, Amer. Meteor. Soc., 7.12. [Available online at https://ams.confex.com/ams/AugAspen/techprogram/paper_14920.htm.]

Ansorge, C., and J. Mellado, 2014: Global intermittency and collapsing turbulence in the stratified planetary boundary layer. *Bound.-Layer Meteor.,* **153,** 89–116, doi:10.1007/s10546-014-9941-3.

Baas, P., G. S. Steeneveld, B. van de Wiel, and A. Holtslag, 2006: Exploring self-correlation in flux–gradient relationships for stably stratified conditions. *J. Atmos. Sci.,* **63,** 3045–3054, doi:10.1175/JAS3778.1.

——, B. van de Wiel, L. van den Brink, and A. Holtslag, 2012: Composite hodographs and inertial oscillations in the nocturnal boundary layer. *Quart. J. Roy. Meteor. Soc.,* **138,** 528–535, doi:10.1002/qj.941.

Basu, S., A. A. Holtslag, B. J. van de Wiel, A. F. Moene, and G.-J. Steeneveld, 2008: An inconvenient "truth" about using sensible heat flux as a surface boundary condition in models under stably stratified regimes. *Acta Geophys.,* **56,** 88–99, doi:10.2478/s11600-007-0038-y.

Beljaars, A., and F. Bosveld, 1997: Cabauw data for the validation of land surface parameterization schemes. *J. Climate,* **10,** 1172–1193, doi:10.1175/1520-0442(1997)010<1172:CDFTVO>2.0.CO;2.

Blackadar, A., 1957: Boundary layer wind maxima and their significance for the growth of nocturnal inversions. *Bull. Amer. Meteor. Soc.,* **38,** 283–290.

Bosveld, F., cited 2014: Observations -> documentation: Cabauw observational program on landsurface-atmosphere interaction (2000 - today). [Available online at http://www.knmi.nl/~bosveld/.]

Businger, J. A., J. C. Wyngaard, Y. Izumi, and E. F. Bradley, 1971: Flux-profile relationships in the atmospheric boundary layer. *J. Atmos. Sci.,* **28,** 181–189, doi:10.1175/1520-0469(1971)028<0181:FPRITA>2.0.CO;2.

Derbyshire, S., 1999: Boundary-layer decoupling over cold surfaces as a physical boundary-instability. *Bound.-Layer Meteor.,* **90,** 297–325, doi:10.1023/A:1001710014316.

Donda, J., B. van de Wiel, I. van Hooijdonk, A. Moene, H. Jonker, G. van Heijst, and H. Clercx, 2015: Collapse of turbulence in stably stratified channel flow: A transient phenomenon. *Quart. J. Roy. Meteor. Soc.,* in press.

Edwards, J. M., 2009: Radiative processes in the stable boundary layer: Part II. The development of the nocturnal boundary layer. *Bound.-Layer Meteor.,* **131,** 127–146, doi:10.1007/s10546-009-9363-9.

Flores, O., and J. Riley, 2011: Analysis of turbulence collapse in the stably stratified surface layer using direct numerical simulations. *Bound.-Layer Meteor.,* **139,** 241–259, doi:10.1007/s10546-011-9588-2.

Galperin, B., S. Sukoriansky, and P. S. Anderson, 2007: On the critical Richardson number in stably stratified turbulence. *Atmos. Sci. Lett.,* **8,** 65–69, doi:10.1002/asl.153.

Grachev, A., C. Fairall, P. Persson, E. Andreas, and P. Guest, 2005: Stable boundary-layer regimes: The SHEBA data. *Bound.-Layer Meteor.,* **116,** 201–235, doi:10.1007/s10546-004-2729-0.

Holtslag, A., and H. de Bruin, 1988: Applied modeling of the nighttime surface energy balance over land. *J. Appl. Meteor.,* **27,** 689–704, doi:10.1175/1520-0450(1988)027<0689:AMOTNS>2.0.CO;2.

Jiménez, M., and J. Cuxart, 2005: Large-eddy simulations of the stable boundary layer using the standard Kolmogorov theory: Range of applicability. *Bound.-Layer Meteor.,* **115,** 241–261, doi:10.1007/s10546-004-3470-4.

King, J. C., and W. M. Connolley, 1997: Validation of the surface energy balance over the Antarctic ice sheets in the U.K. Meteorological Office Unified Climate Model. *J. Climate,* **10,** 1273–1287, doi:10.1175/1520-0442(1997)010<1273:VOTSEB>2.0.CO;2.

——, S. D. Mobbs, and N. R. Edwards, 1994: Surface boundary conditions in stably-stratified environmental flows. *Stably Stratified Flows: Flow and Dispersion over Topography,* I. P. Castro and N. J. Rockliff, Eds., Clarendon Press, 93–103.

Klipp, C. L., and L. Mahrt, 2004: Flux–gradient relationship, self-correlation and intermittency in the stable boundary layer. *Quart. J. Roy. Meteor. Soc.,* **130,** 2087–2103, doi:10.1256/qj.03.161.

Łobocki, L., 2013: Analysis of vertical turbulent heat flux limit in stable conditions with a local equilibrium, turbulence closure model. *Bound.-Layer Meteor.,* **148,** 541–555, doi:10.1007/s10546-013-9836-8.

Louis, J., 1979: A parametric model of vertical eddy fluxes in the atmosphere. *Bound.-Layer Meteor.,* **17,** 187–202, doi:10.1007/BF00117978.

Mahrt, L., 2014: Stably stratified atmospheric boundary layers. *Annu. Rev. Fluid Mech.,* **46,** 23–45, doi:10.1146/annurev-fluid-010313-141354.

——, J. Sun, W. Blumen, T. Delany, and S. Oncley, 1998: Nocturnal boundary-layer regimes. *Bound.-Layer Meteor.,* **88,** 255–278, doi:10.1023/A:1001171313493.

Malhi, Y. S., 1995: The significance of the dual solutions for heat measured by the temperature fluctuation method in stable conditions. *Bound.-Layer Meteor.,* **74,** 389–396, doi:10.1007/BF00712379.

Mauritsen, T., G. Svensson, S. Zilitinkevich, I. Esau, L. Enger, and B. Grisogono, 2007: A total turbulent energy closure model for neutrally and stably stratified atmospheric boundary layers. *J. Atmos. Sci.,* **64,** 4113–4126, doi:10.1175/2007JAS2294.1.

McNider, R., D. England, M. Friedman, and X. Shi, 1995: Predictability of the stable atmospheric boundary layer. *J. Atmos. Sci.,* **52,** 1602–1614, doi:10.1175/1520-0469(1995)052<1602:POTSAB>2.0.CO;2.

Monahan, A. H., Y. He, N. McFarlane, and A. Dai, 2011: The probability distribution of land surface winds. *J. Climate,* **24,** 3892–3909, doi:10.1175/2011JCLI4106.1.

Monin, A., and A. Obukhov, 1954: Basic laws of turbulent mixing in the atmosphere near the ground. *Tr. Akad. Nauk., SSSR Geofiz. Inst.,* **24,** 1963–1987.

Monteith, J. L., 1981: Evaporation and surface temperature. *Quart. J. Roy. Meteor. Soc.,* **107,** 1–27, doi:10.1002/qj.49710745102.

Nieuwstadt, F., 2005: Direct numerical simulation of stable channel flow at large stability. *Bound.-Layer Meteor.,* **116,** 277–299, doi:10.1007/s10546-004-2818-0.

Sorbjan, Z., 2006: Local structure of turbulence in stably stratified boundary layers. *J. Atmos. Sci.,* **63,** 1526–1537, doi:10.1175/JAS3704.1.

Stull, R., 2000: *Meteorology for Scientists and Engineers*. 2nd ed. Brooks/Cole, 502 pp.

Sun, J., and Coauthors, 2004: Atmospheric disturbances that generate intermittent turbulence in nocturnal boundary layers. *Bound.-Layer Meteor.,* **110,** 255–279, doi:10.1023/A:1026097926169.

——, L. Mahrt, R. Banta, and Y. Pichugina, 2012: Turbulence regimes and turbulence intermittency in the stable boundary layer during CASES-99. *J. Atmos. Sci.,* **69,** 338–351, doi:10.1175/JAS-D-11-082.1.

Taylor, P. A., 1971: A note on the log-linear velocity profile in stable conditions. *Quart. J. Roy. Meteor. Soc.,* **97,** 326–329, doi:10.1002/qj.49709741308.

van de Wiel, B., A. Moene, G. Steeneveld, P. Baas, F. Bosveld, and A. Holtslag, 2003: Intermittent turbulence and oscillations in the stable boundary layer over land. Part III: A classification for observations during CASES-99. *J. Atmos. Sci.,* **60,** 2509–2522, doi:10.1175/1520-0469(2003)060<2509:ITITSB>2.0.CO;2.

——, ——, ——, O. Hartogensis, and A. Holtslag, 2007: Predicting the collapse of turbulence in stably stratified boundary layers. *Flow Turbul. Combust.,* **79,** 251–274, doi:10.1007/s10494-007-9094-2.

——, ——, W. Ronde, and H. Jonker, 2008: Local similarity in the stable boundary layer and mixing-length approach: Consistency of concepts. *Bound.-Layer Meteor.,* **128,** 103–116, doi:10.1007/s10546-008-9277-y.

——, ——, and H. Jonker, 2012a: The cessation of continuous turbulence as precursor of the very stable nocturnal boundary layer. *J. Atmos. Sci.,* **69,** 3097–3115, doi:10.1175/JAS-D-12-064.1.

——, ——, ——, P. Baas, S. Basu, J. Donda, J. Sun, and A. Holtslag, 2012b: The minimum wind speed for sustainable turbulence in the nocturnal boundary layer. *J. Atmos. Sci.,* **69,** 3116–3127, doi:10.1175/JAS-D-12-0107.1.

van Ulden, A., and J. Wieringa, 1996: Atmospheric boundary layer research at Cabauw. *Bound.-Layer Meteor.,* **78,** 39–69, doi:10.1007/BF00122486.

Wang, J., and R. Bras, 2010: An extremum solution of the Monin–Obukhov similarity equations. *J. Atmos. Sci.,* **67,** 485–499, doi:10.1175/2009JAS3117.1.

Zilitinkevich, S. S., T. Elperin, N. Kleeorin, I. Rogachevskii, I. Esau, T. Mauritsen, and M. W. Miles, 2008: Turbulence energetics in stably stratified geophysical flows: Strong and weak mixing regimes. *Quart. J. Roy. Meteor. Soc.,* **134,** 793–799, doi:10.1002/qj.264.